Journal of Solid State Electrochemistry (2021) 25:207–217
https://doi.org/10.1007/s10008-020-04729-5

ORIGINAL PAPER

Glucose oxidation reaction at palladium-carbon nano-onions in alkaline media

Carlos A. Vélez[1] · Joesene J. Soto-Pérez[1] · Juan Corchado-García[1] · Eduardo Larios[1,2] · Pasquale F. Fulvio[3] · Luis Echegoyen[4] · Carlos R. Cabrera[1]

Received: 20 May 2020 / Revised: 15 June 2020 / Accepted: 15 June 2020 / Published online: 2 July 2020

Abstract

The glucose oxidation reaction, at Pd on unsupported carbon nano-onions (Pd/CNOs), has been studied by using physical and electrochemical characterization techniques. The rotating disk slurry electrode (RoDSE) technique was used for the Pd electrodeposition at the carbon support. The Pd/CNO catalyst was compared with the optimized RoDSE-prepared Pd/Vulcan XC-72R nanoflake catalyst for the glucose oxidation reaction by using different physical and electrochemical characterization techniques. Powder XRD analysis verified the effect of the carbon support material on the Pd crystallinity and size nanoparticles. Raman spectroscopy and X-ray photoelectron spectroscopy were used to understand the chemical structure of each carbon support before and after the Pd electrodeposition. The surface area and porosity of both Pd/C catalysts and their respective carbon substrates were investigated using N_2 adsorption analysis. Transmission electron microscopy images established the morphology and the sizes of the Pd/CNOs, obtaining a large dispersion of nanoparticles with an average diameter size between 35 and 40 nm, with smaller particles in the range between 2 and 10 nm. Finally, cyclic voltammetry (CV) and linear sweep voltammetry (LSV) were used to compare the electrocatalytic activity of Pd/C, Vulcan XC-72R, and CNOs, for the glucose oxidation reaction in alkaline media. The results indicate that Pd/CNOs has the capacity to oxidize glucose in the normal glucose range between 5 and 8 mM, the normal range of glucose in human blood.

Keywords RoDSE · Pd catalyst · CNOs · Glucose oxidation

Introduction

Diabetes mellitus is a genetically heterogeneous group of disorders that exhibit glucose intolerance [1]. Diabetes is mostly characterized by chronic hyperglycemia with a perturbation of carbohydrate, fat, and protein metabolism. The most common way to classify this disorder is either by the body's inadequate production of insulin (type 1) or by the body's incapacity to use the insulin it produces (type 2). Insulin is the hormone that regulates the levels of glucose in the bloodstream. Excessive amounts of glucose in the blood can cause cardiovascular, cerebrovascular, and peripheral vascular diseases [2]. It is known that this disease affects nearly 3% of the global population and is expected to rise even more in the future [3]. While there is no cure for diabetes, the common approach is to keep the disorder under control and to monitor the glucose levels in the patient's blood, tears, and skin. The monitoring is commonly done using a glucose-sensitive sensor.

Clark and Lyons introduced glucose sensors in 1962 [4]. They monitored oxygen consumption by measuring glucose oxidation with an enzyme called glucose oxidase (GOx). This enzyme catalyzes the reduction of O_2 to H_2O_2 and gluconic acid in the presence of glucose (reaction 1) with the use of a working electrode, in this report it was a platinum electrode.

$$\text{glucose} + O_2 \rightarrow^{GOx} \text{gluconic acid} + H_2O_2 \quad (1)$$

They measured the rate of this reaction because it is proportional to the concentration of glucose and the increment of H_2O_2 concentration [5]. But, they confronted problems related to the oxygen requirements. If samples were deficient in

✉ Carlos R. Cabrera
carlos.cabrera2@upr.edu

[1] Department of Chemistry, University of Puerto Rico, Río Piedras Campus, San Juan, PR 00925-2537, USA

[2] Departamento de Ingeniería Química y Metalurgia, Universidad de Sonora, 83000 Hermosillo, Mexico

[3] Department of Nuclear Engineering, Texas A&M University, College Station, TX 77843, USA

[4] Department of Chemistry and Biochemistry, University of Texas at El Paso, El Paso, TX 79968, USA

oxygen, they would not give an accurate result. The sensor also interfered with electroactive species such as uric acid, ascorbic acid, and drugs that could be present in the blood like acetaminophen, dopamine, and amphetamines [6]. Updike and Hicks fixed this problem with another sensor in 1967. They stabilized glucose oxidase and added another working sensor to measure the differential current and, therefore, to correct the variations of oxygen levels in the sample [7]. After making the first amperometric sensor in 1973 [8], scientists started cataloging the sensors by generations. They developed four generations. The first three generations were dependent on enzymes, such as glucose 1-oxidase (GOx) or glucose dehydrogenase (GDH). Even with the high selectivity that enzyme-based detectors have, the nature of the enzymes affects the reproducibility and sensitivity of such sensors. Such drawbacks compel the consumer to buy a new sensor after each use, thus making the technology very expensive [3, 6, 9].

The glucose sensor industry improved the stability through these three generations, but enzymatic sensors were not reliable in oxidizing glucose, and researchers decided to create non-enzymatic sensors, cataloged as the fourth-generation glucose sensors.

Non-enzymatic glucose sensing, in which glucose is directly oxidized on the surface of the electrode, provides excellent sensitivity and reproducibility while avoiding the fragility and complex immobilization processes needed for enzymes on electrode surfaces [6, 10–14]. A diversity of catalysts, based on noble metals and metal oxides such as Pt [15–17], Au [18], CuO/Cu_2O [19–22], and NiO [23, 24], has been studied for commercial non-enzymatic glucose sensors (NEGS). Recently, Pd-based catalysts have emerged as a possible candidate for NEGS, showing excellent activity towards glucose oxidation in alkaline media [25–28].

Because of their properties, carbon substrates are an ideal support material to increase electrocatalytic activity and at the same time to minimize the amount of metal used for a given reaction [29–32]. Echegoyen et al. [33] have prepared functionalized carbon nano-onions (CNOs) consisting of a few carbon shells with an overall diameter between 4 and 8 nm; by vacuum annealing ultradispersed nanodiamonds, oxygen functionalities on the carbon surface have been introduced via acid treatment [34]. Recently, Santiago et al. [35] were able to deposit Pt nanoparticles on these functionalized CNO supports and produced Pt–based catalysts with enhanced electrocatalytic activity towards methanol oxidation. Cunci et al. [36] showed the efficient electrodeposition of these Pt-CNOs on reduced graphene oxide to catalyze the ammonia oxidation reaction. In this work, Pd nanoparticles were deposited on the oxidized CNOs by using the rotating disk slurry electrode (RoDSE) methodology using the optimized conditions described by Vélez et al. [36]. The Pd/CNO catalyst was used to oxidize glucose, and the results were compared with that for optimized Pd/Vulcan XC-72R catalyst.

Experimental methodology

Materials

Potassium hydroxide (KOH), palladium (II) chloride ($PdCl_2$), Nafion solution (5% solution in ethanol (EtOH)), isopropanol, EtOH (99.5%), and sulfuric acid (H_2SO_4) were purchased from Sigma Aldrich. Vulcan XC-72R (BASF), and alumina 1, 0.3, and 0.05 μm were purchased from Buehler Micropolish.

Catalyst preparation

Carbon nano-onions

Oxidized CNOs with an average size of 5 nm were prepared as previously described by Echegoyen et al. [33, 34, 37] Briefly, annealing of nanodiamonds with a crystal size between 4 and 6 nm was done at 1650 °C under a 1.1-MPa He atmosphere. After the furnace was opened, the CNO product was annealed in air at 400 °C to remove any amorphous carbon. The functionalization of the CNOs was done by dispersing and subsequently refluxing the carbon material for 48 h in a 3.0-M nitric acid solution. Afterwards, the mixture was centrifuged for 10 min to obtain a black powder. Finally, to purify the oxidized CNOs, the carbon material was stirred in a 3.0-M NaOH solution, washed several times with water until a pH of 7 was reached, and dried at 110 °C overnight.

Preparation of the Pd/CNO and Pd/Vulcan XC-72R nanoflake catalysts

These two catalysts were prepared using the RoDSE methodology. Typically, a 50-mg suspension of the corresponding carbon support material with 20 mL of 0.1-M H_2SO_4 was made in a beaker and sonicated for 8 h. The preparation of each Pd/C catalyst was done by applying a constant electrodeposition potential to a rotating disk electrode (RDE) of glassy carbon (GC) (PINE research instrumentation) with an area of 0.1963 cm^2, while rotating it at 1200 rpm. The potential applied was 0.4 V vs. reversible hydrogen electrode (RHE) for 2 h, after every addition (4 times) of a 2.00-mL aliquot of a 5.0-mM $PdCl_2$/0.1-M H_2SO_4 solution to the carbon slurry. After the final electrodeposition, the corresponding slurry was filtered through a 0.22-μm Nylon filter and washed with abundant deionized water. The resulting material was dried at 60 °C in an oven for 24 h and ground to obtain a fine powder. The Pd loading measured by thermal gravimetric analysis (TGA) for Pd/CNO and Pd/Vulcan was 9% and 8% by weight, respectively.

Electrochemical measurements

The ink preparation of each analysis consisted of 3 mg of catalyst powder, 150 μL of deionized water, 150 μL of isopropanol, 300 μL of ethanol, and 5 μL of 5% Nafion solution in EtOH. All the reagents were sonicated for 1 h to form the ink paste. Later, a glassy carbon electrode (GCE, 3-mm diameter, BASi) was cleaned three times with 1.0-, 0.3-, and 0.05-μm alumina powder, rinsed with deionized water, and sonicated for 10 min to remove alumina residues. Subsequently, an electrochemical cleaning was executed at − 0.1–1.1 V vs. Ag/AgCl at 100 mV/s, 50 mV/s, and 20 mV/s in KOH (0.1 M). Finally, 5 μL of the ink paste was dropped on the GCE surface and dried at 60 °C in an oven for 120 s.

Electrochemical characterization for each Pd/C catalyst was carried out under ambient conditions using cyclic voltammetry (CV) and linear sweep voltammetry (LSV) in alkaline media. All measurements were done using a BioLogic SP-200 potentiostat. In all experiments, a three-electrode cell was employed consisting of a Pt auxiliary electrode, RHE as reference electrode, and a modified GCE as the working electrode.

Physical characterization

X-ray powder diffraction (XRD) was utilized to determine the chemical composition and crystallographic structure of each Pd/C catalyst and their respective carbon support substrate. XRD patterns, for Pd/CNOs, Pd/Vulcan XC-72R nanoflakes, and their respective carbon supports were obtained on a Rigaku SmartLab X-ray diffractometer working with the Cu K_α radiation ($\lambda = 1.54$ Å). The 2 range was scanned between 10 and 80° at a rate of 0.02° s^{-1}.

Raman spectroscopy was utilized to probe the chemical structure of each carbon support substrate before and after Pd electrodeposition. Room-temperature Raman spectra were investigated at wavelengths between 900 and 3000 cm^{-1} using a Thermo Scientific DXR Raman Microscope with a 532-nm laser line. To avoid sample burning, the power of the laser beam was placed at 5.0 mW.

To further understand the chemical structure of each carbon support, each Pd/C catalyst and their respective carbon substrate were studied by X-ray photoelectron spectroscopy (XPS). High binding energy resolution (high resolution X-ray photoelectron spectroscopy (HR-XPS)) spectra of C 1s were analyzed using a fitting program (Multipack, Physical Electronics) for peak deconvolution. X-ray photoelectron spectroscopy (XPS) spectra were obtained using a PHI 5600ci spectrometer equipped with an aluminum polychromatic source (350 W) at a 45° angle and a hemispherical electron energy analyzer. The pass energy was 58.70 eV. A small sample of the catalytic powder was pressed onto copper tapes.

The 200-kV field emission FEI F20 transmission electron microscopy (TEM) SEM from the facilities of the Cornel Center for Materials Research (CCMR) at Cornell University was used to study the morphology and determine the sizes of the Pd/CNO nanoparticles. These samples were prepared on a lacey carbon film of 300-mesh Cu grid (electron microscopy sciences, EMS).

The adsorption properties such as surface area and pore size analysis for each Pd/C catalyst and their respective carbon support were examined with N_2 at − 196 °C by using the volumetric TriStar II 3020 from Micrometrics® automatic surface area and porosity analyzer. The specific surface areas (S_{BET}) were calculated using the Brunauer, Emmett, and Teller (BET) equation within the relative pressure range of 0.05–0.20 [38]. Single-point pore volumes (V_{SP}) were obtained directly from the adsorption isotherms at the relative pressure of 0.85. Micropore volumes (V_{mi}) and micropore surface areas (S_{mi}) were calculated using the t-plot method; t-plot curves were calculated using the carbon black STSA equation [39, 40]. Average pore widths were obtained from the geometrical relation for slit-like pores, the single-point pore volume, and BET surface areas. All the data obtained was plotted using the Origin software.

Results and discussion

Pd electrodeposition on CNOs and Vulcan XC-72R nanoflakes

In our previous work, 0.4 V vs. RHE was determined as an ideal electrodeposition potential to deposit Pd nanoparticles on Vulcan XC-72R nanoflakes while employing the RoDSE methodology [41]. These electrodeposition conditions optimize particle sizes and metal yields of the deposited Pd nanoparticles. Because of this, 0.4 V vs. RHE was applied for the deposition of Pd nanoparticles on CNO substrates and compared with that of Vulcan XC-72R nanoflakes. Figure 1 demonstrates the successful deposition of Pd on CNOs and Vulcan XC-72R nanoflakes by using the RoDSE technique at an applied electrodeposition potential of 0.4 V vs. RHE. Notably, the average electrodeposition currents obtained with both carbon support materials are comparable (− 0.73 and − 0.68) A for CNOs and Vulcan XC-72R nanoflakes, respectively). These results suggest that the electrodeposition of Pd by using the RoDSE methodology, using the same conditions described in previous work, occurs in an analogous manner at CNOs and Vulcan XC-72R nanoflake support material.

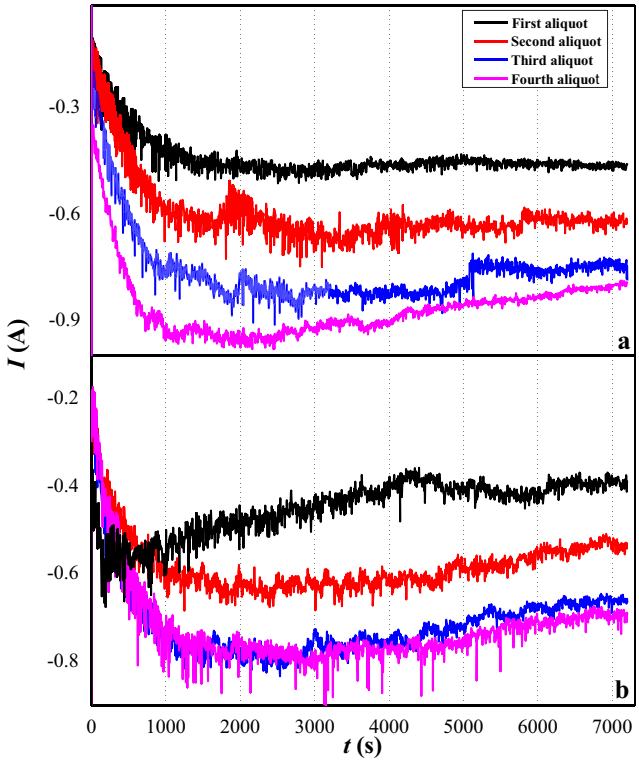

Fig. 1 Current vs. time graphs for Pd electrodeposition in 20 mL of a CNO (A) and Vulcan XC-72R nanoflake (B) slurry in 0.1-M H_2SO_4 at an applied electrodeposition potential of 0.4 V vs. RHE. For each applied potential, four consecutive electrodepositions were done. In each electrodeposition, a 2-mL aliquot of a 5-mM $PdCl_2$/0.1-M H_2SO_4 solution was added to the slurry solution

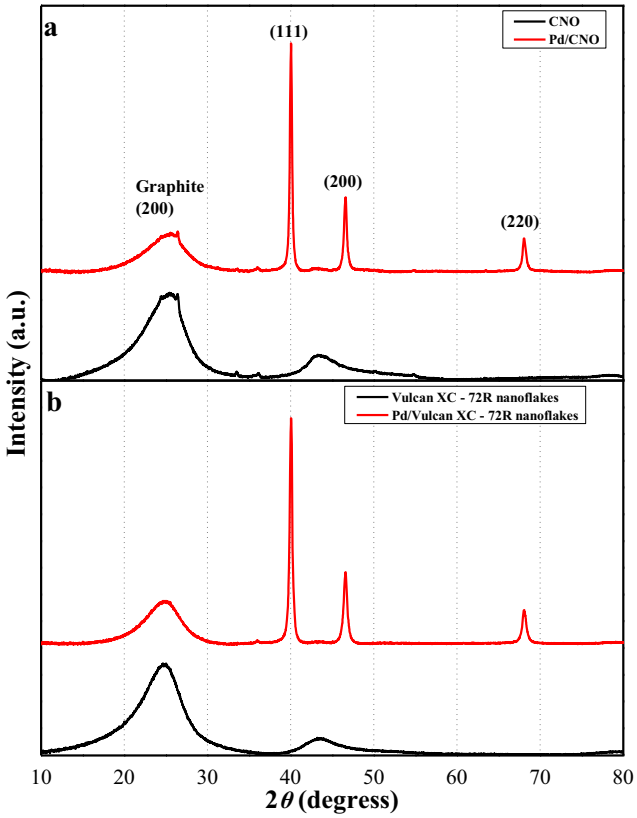

Fig. 2 XRD patterns for the Pd/CNO (A) and Pd/Vulcan XC-72R nanoflake (B) catalysts synthesized by using the RoDSE methodology at 0.4 V vs. RHE applied electrodeposition potential

X-ray diffraction measurements

XRD analysis was recorded for the CNOs and Vulcan XC-72R nanoflake carbon supports before and after Pd electrodeposition. XRD patterns of all samples (Fig. 2) show three peaks at 2 = 40.0°, 46.5°, and 68.1° corresponding to the (111), (200), and (220) planes of the Pd face center cubic structure, respectively [42]. A broad peak appears at ~25°, where the (002) interplanar spacing reflection of graphite is expected. The broadening and low intensity of this peak, as compared with graphite, indicates the low degree of correspondence between graphene planes in the present carbon supports (turbostratic structure). The XRD results confirm the successful deposition of crystalline palladium on both CNOs and Vulcan XC-72R nanoflakes without affecting the crystalline lattice of either carbon support.

Raman spectroscopy

Raman spectroscopy was used to probe the effect of the carbon substrate on the deposition of Pd nanoparticles employing the RoDSE methodology. Figure 3 shows the Raman spectra of CNOs (A) and Vulcan XC-72R nanoflakes (B) before (black) and after (red) Pd deposition via the RoDSE methodology. Both carbon support materials show two bands around 1350 and 1580 cm^{-1}, which correspond to the respective D and G bands from the graphene E_{2g} lattice modes. It is important to mention that a broad third component was observed for the Vulcan XC-72R nanoflake carbon substrate, at around 1500–1550 cm^{-1}, which is assigned to amorphous carbon. For the Raman spectra, no bands can be discerned from 1800 to 2300 cm^{-1}. For the CNO support, a second-order Raman characteristic of graphite and carbon materials sharing an extended two-dimensional hexagonal sp^2 carbon lattice can be seen from 2350 to 3000 cm^{-1}. The overriding Raman band at around 2700 cm^{-1} corresponds to an overtone of the first-order peak at 1350 cm^{-1} [43]. A small peak at 1100 cm^{-1} is observed for the oxidized CNOs before Pd deposition. This peak is attributed to the presence of sp^3–sp^3 stretching in the carbon material [44]. However, after Pd deposition, this peak is not observed. In contrast, for the Vulcan XC-72R nanoflake carbon substrate, the peak at 1100 cm^{-1} can be observed after Pd electrodeposition.

As mentioned earlier, it was demonstrated that applying an electrodeposition potential of 0.4 V vs. RHE for the deposition of Pd nanoparticles using the RoDSE technique resulted in the partial oxidation of the Vulcan XC-72R nanoflake carbon support [41]. This partial oxidation contributes to the formation of sp^3 carbon atoms and thus the 1100-cm^{-1} Raman peak.

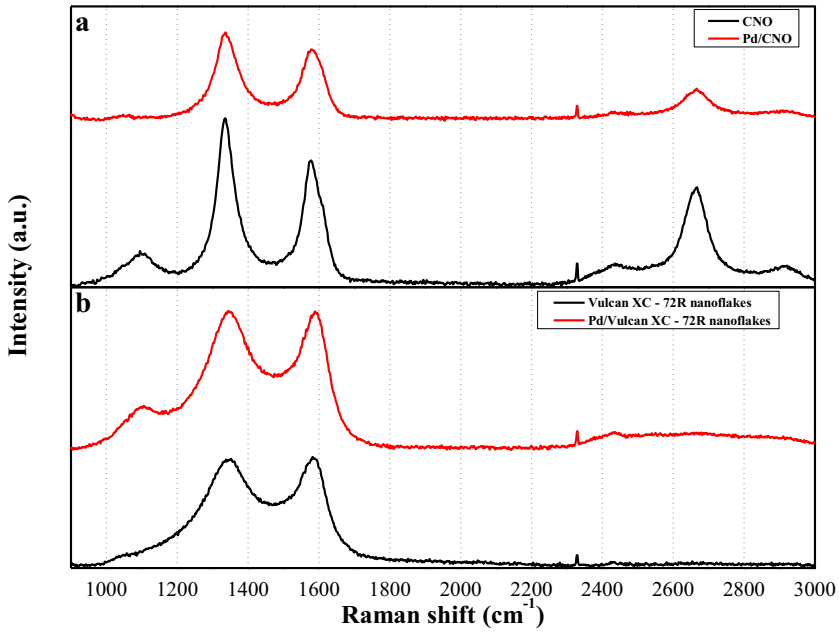

Fig. 3 Raman spectra of the CNO (A) and Vulcan XC-72R nanoflake (B) carbon substrate before (black) and after (red) Pd electrodeposition via the RoDSE methodology

Likewise, the oxygen functionalities introduced during the preparation of the CNO substrate may contribute to the same Raman peak. Data from Fig. 3 suggests that after Pd deposition, the CNO and Vulcan XC-72R nanoflake carbon supports are partially reduced and oxidized, respectively. Because CNOs have mainly graphene carbon domains and Vulcan XC-72R has a significant amount of amorphous carbon, these results suggest that the morphology of the carbon substrate is a key factor in the deposition of Pd nanoparticles employing the RoDSE methodology.

X-ray photoelectron spectroscopy

HR-XPS spectra at the C 1s binding energy region of CNOs and Vulcan XC-72R nanoflakes, before and after Pd electrodeposition, are shown in Fig. 4. Peak assignments for the C 1s components are shown in Table 1 [41, 45]. The XPS results for C 1s binding energy regions were analyzed using a curve-fitting program (Multipack) for peak deconvolution. The features around 284.3 eV correspond to sp^2 carbons [41, 45] and can be used to compare the degree of oxidation among samples; stronger sp^2 carbon peaks correspond to a more reduced carbon support and better ordering of the graphene lattice within these particles. The pristine supports show a marked difference, with the CNOs having much sharper features in the ordered region than Vulcan XC-72R nanoflakes. The CNO spectrum shows a clear separation between sp^2 and sp^3 carbons, whereas in the Vulcan XC-72R nanoflakes, the ordered graphene contribution is seen as a shoulder of the sp^3 carbon peak.

The carbon 1s binding energy spectra region show increased graphene in plane carbon contribution after electrodeposition in both supports. The Pd/Vulcan XC-72R nanoflakes show a slight increase in the ordered carbon region compared with the respective pristine carbon support. This is in sharp contrast to the Pd/CNO spectrum, where it is almost completely dominated by the sp^2-ordered carbon signal. The difference in composition between the two supports after electrodeposition agrees closely with the Raman analysis. The difference in graphene carbon intensity leads us to believe that the applied potential is highly reducing for the CNOs but only slightly reducing for the Vulcan XC-72R nanoflakes.

Gas adsorption measurements

The adsorption properties for CNOs and Vulcan XC-72R nanoflakes were investigated using nitrogen gas at − 196 °C. The adsorption isotherms are presented in Fig. 5 and are classified as type II, characteristic of macroporous solids (pore widths > 50 nm), with hysteresis loops resembling very large slit-like pores. The higher amount of gas uptake at low relative pressure and the total gas uptake at the relative pressure of 0.85 for the CNO and Pd/CNO samples result from the presence of small textural pores, i.e., micropores (widths < 2 nm) and mesopores (widths between 2 and 50 nm) [38]. The presence of small amounts of micropores was further verified by using the t-plot analysis [39, 40], which were comparable for all samples, as summarized in Table 2. Values also agree with those previously reported for Vulcan that has some additional deep micropores [46].

Besides total pore volume, the BET surface area for CNO materials was more than two times higher than the surface area of Vulcan XC-72R nanoflakes, and for their corresponding Pd composites, as well. This substantial increase in surface areas

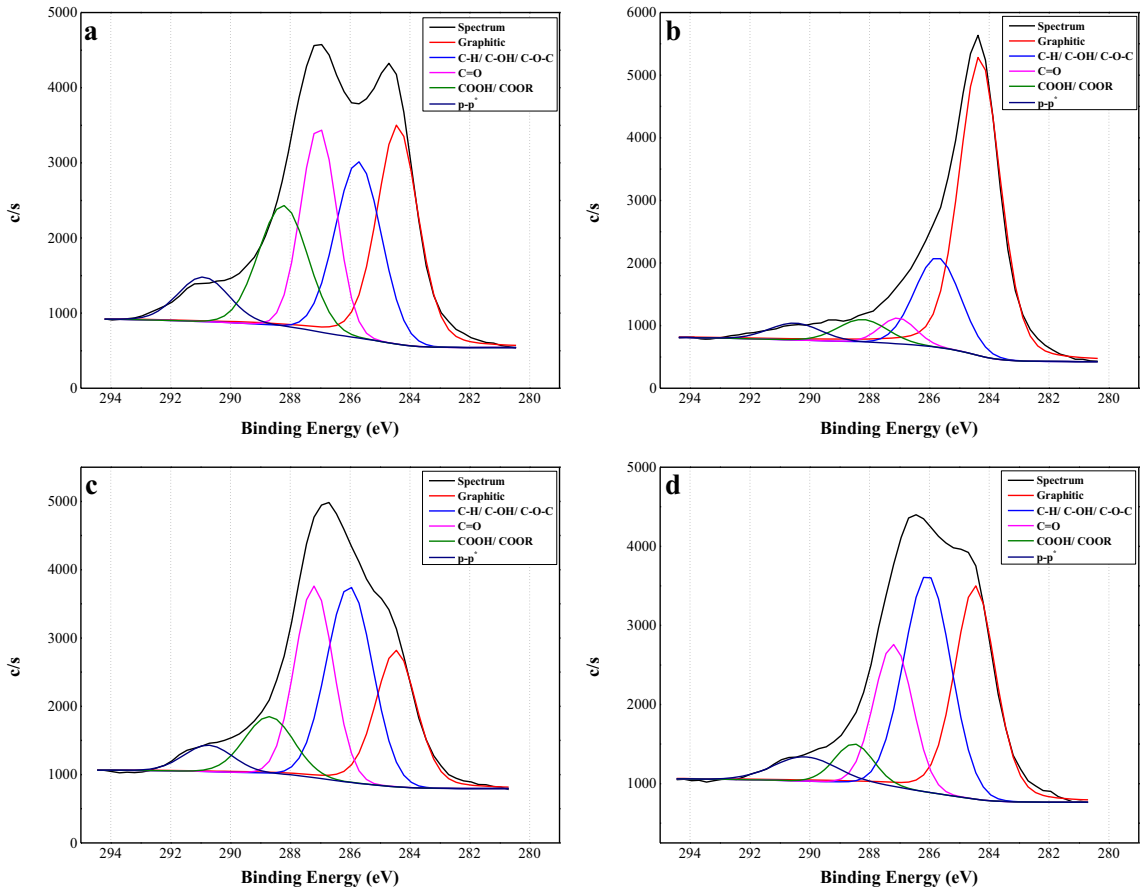

Fig. 4 C 1s binding energy spectra of CNOs (**a**), Pd/CNOs (**b**), Vulcan XC-72R nanoflakes (**c**), and Pd/Vulcan XC-72R nanoflake (**d**) catalysts synthesized by using the RoDSE methodology

was most likely the consequence of small textural mesopores present in the CNO materials. For instance, assuming a slit-like pore geometry, the total pore volume and BET surface area (total surface area) for the CNO materials have an approximate pore width of 3 nm compared with 160 nm for the mostly macroporous Vulcan XC-72R nanoflakes. Overall, the samples with Pd had slightly lower adsorption parameters than their carbon counterparts. This result is expected, due to the added weight of Pd to the CNO and Vulcan-72R composites. Finally, the higher surface area of the Pd/CNOs suggests that the Pd catalyst will be more accessible to affect a catalytic reaction and will consequently be a more active material than the Pd/Vulcan XC-72R nanoflake composites.

Table 1 Binding energy peak assignment for the C 1s components

Carbon 1s components	Binding energy (eV)
Graphite (sp^2)	~284.4
C-H (sp^3)/C-OH/C-O-C	~285.4
C=O	~287.6
COOH/COOR	~289.1
π-π^*	~291.0

Transmission electron microscopy measurements

TEM corroborates the presence of Pd nanoparticles (Pd-Nps) dispersed on CNOs with a large polydispersity of particle sizes. Figure 6 a and e show mainly Pd-Nps in the 35–40-nm range, and Fig. 1 (SI) shows TEM images of bare CNO for comparison. However, these large particles are aggregates of smaller particles, as can be seen in b, c, and f. Smaller particles are seen between 2 and 10 nm in Fig. 6 d, g, and h. The energy dispersive spectrum (EDS) shown in Fig. 6j shows the presence of Pd in the sample. In Fig. 6i, we can observe from the high-angle annular dark field (HAADF) image that the metallic nanoparticles (Pd) have notably greater contrast with respect to the carbon support (CNOs). A histogram (k) plot of the particle sizes shows the large dispersion in diameters, although this large dispersion may be due to the aggregation of smaller Pd-Nps as shown in Fig. 6b, c, and f.

Electrochemical measurements

The electrocatalytic activities towards glucose oxidation in alkaline media for the Pd/CNOs and Pd/Vulcan XC-72R nanoflake catalysts were tested by using cyclic and linear sweep

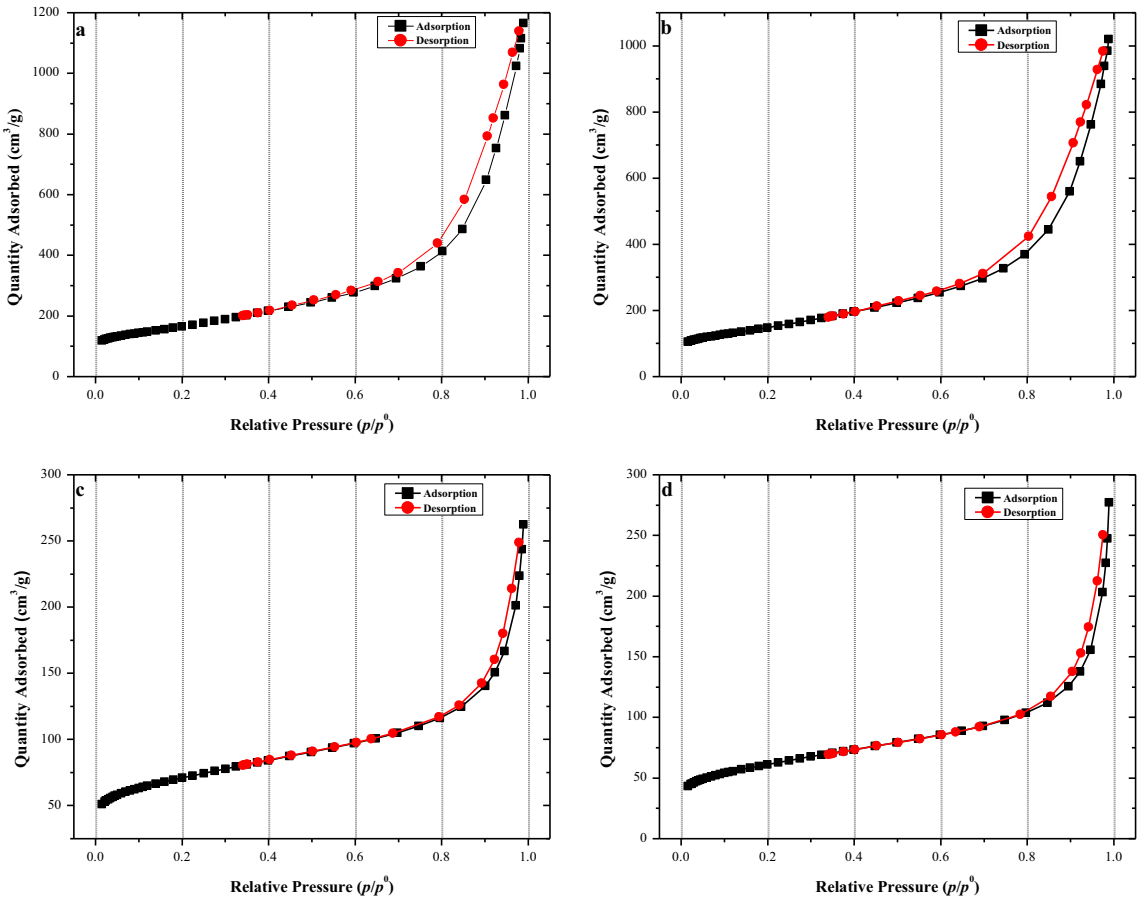

Fig. 5 Nitrogen adsorption isotherm of **a** CNOs, **b** Pd/CNOs, **c** Vulcan XC-72R nanoflakes, and **d** Pd/Vulcan XC-72R nanoflakes

voltammetry. Figure 7 shows cyclic voltammograms in 0.1-M KOH of modified glassy carbon electrodes with Pd/CNOs and Pd/Vulcan XC-72R. The cathodic peaks observed at 0.65 V vs. RHE are due to the reduction of the PdO monolayer formed in the anodic sweep [47]. The primary differences in the voltammograms consist in that the capacitance double-layer current of Pd/CNOs is considerably higher than that for Pd/Vulcan XC-72R nanoflake catalyst. Because the capacitance current is directly related to the active surface area of the carbon support substrate [47], these measurements are in agreement with the BET results, where Pd/CNO was found to have more than double the surface area of Pd/Vulcan XC-72R nanoflake.

The catalytic activity for each Pd/Vulcan XC-72R nanoflake catalyst was examined by linear sweep voltammetry for glucose oxidation in alkaline media (Fig. 8) Both Pd/CNO and Pd/Vulcan XC-72R nanoflake catalysts have similar electrocatalytic activity towards glucose oxidation. However, it is important to mention that Pd/CNO has a slightly higher oxidative current and oxidizes glucose at more negative potentials than Pd/Vulcan XC-72R nanoflakes. These slight variances in the oxidation of glucose may be due to the much higher active surface area of Pd/CNOs in contrast to Pd/Vulcan XC-72R nanoflakes as indirectly probed by the BET results. Furthermore, the higher graphene lattice ordering of the Pd/CNO catalyst particle domains results in more efficient electron transfer due to electron delocalization within the more ordered carbon layers and because of their lower degree of oxidation and lattice defects.

Table 2 CNO and Vulcan XC-72R nanoflake carbon supports physical properties: before and after Pd electrodeposition via the RoDSE methodology in terms of pore volume and diameter from BET surface area analysis

Sample	CNOs	Pd/CNOs	Vulcan XC-72R nanoflakes	Pd/Vulcan XC-72R nanoflakes
V_{SP} (cm^3/g)	0.9	0.84	0.2	0.18
S_{BET} (m^2/g)	584	526	250	218
S_{mi} (m^2/g)	69	40	85	62
V_{mi} (cm^3/g)	0.035	0.021	0.039	0.028
Average pore width (nm)	3.1	3.2	160	162

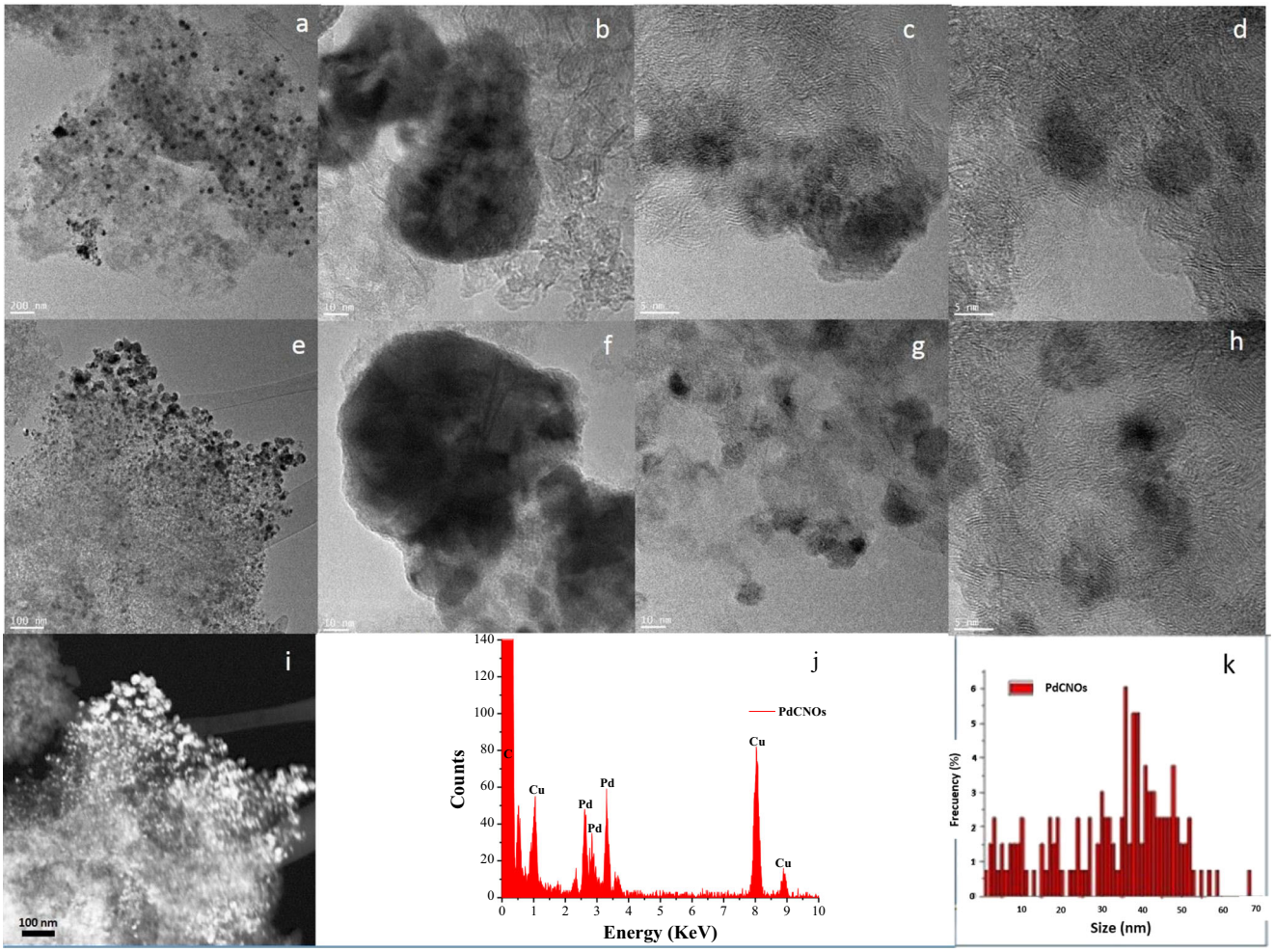

Fig. 6 TEM (**a**–**h**) and STEM-HAADF (**i**) Pd/CNOs synthesized by using the optimized RoDSE method. **j** EDS spectrum of **i** and Pd nanoparticle diameter histogram of the TEM images (**k**)

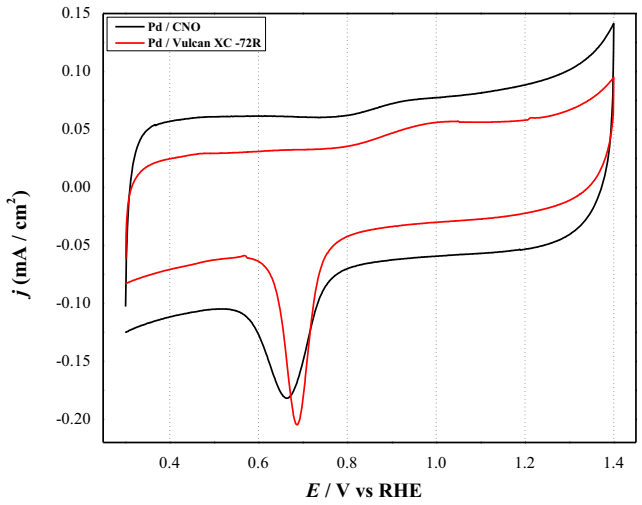

Fig. 7 Cyclic voltammogram in 0.1-M KOH for the Pd/CNO (black) and the Pd/Vulcan XC-72R nanoflake (red) catalysts synthesized by using the RoDSE at 0.4 V vs. RHE applied electrodeposition potential. The scan rate was 25 mV/s

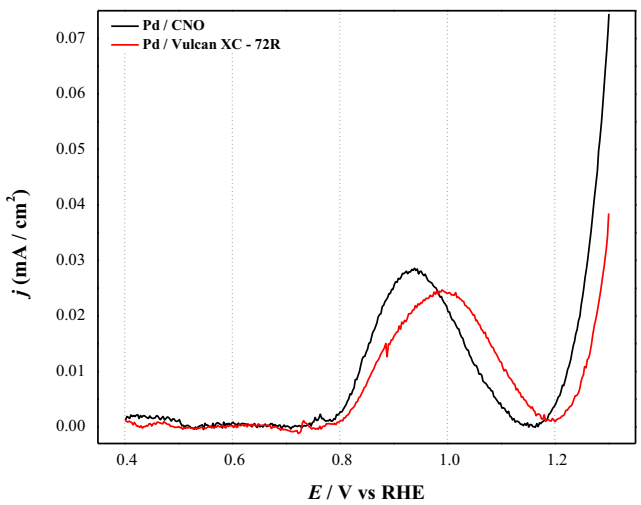

Fig. 8 Linear sweep voltammograms for the Pd/CNO (black) and the optimized Pd/Vulcan XC-72R nanoflake (red) catalysts in 5-mM D-glucose/0.1-M KOH using a scan rate of 25 mV/s

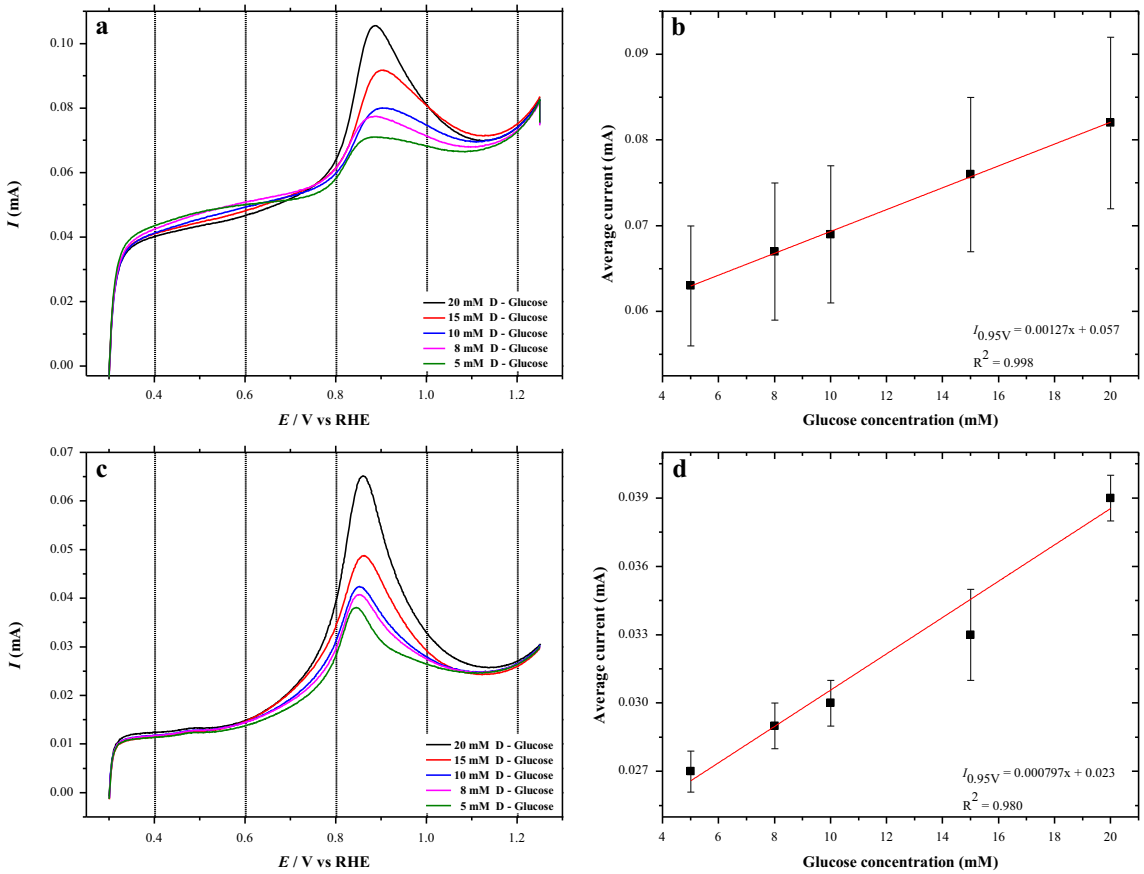

Fig. 9 Linear sweep voltammetry of **a** Pd/CNO and **c** Pd/Vulcan XC-72R nanoflake catalysts in 0.1-M KOH with different concentrations of D-glucose with a scan rate of 25 mV/s and their respective calibration curves (**b**, **d**) at an applied potential of 0.95 V vs. RHE

Glucose electro-oxidation with Pd/CNO and Pd/Vulcan XC-72R nanoflake catalysts was further evaluated by using LSV in 0.1-M KOH in the presence of various concentration of glucose (Fig. 8). Data in Fig. 9 a and c show an increment in the anodic peak current as a function of glucose concentration for both Pd/CNOs and Pd/Vulcan XC-72R nanoflakes. The anodic current at 0.95 V vs. RHE showed a linear relationship with glucose concentration with a correlation coefficient of 0.998 and 0.980 for Pd/CNOs and Pd/Vulcan XC-72R nanoflakes, respectively (Fig. 9 b and d). However, there is a significant variability in the anodic current for the Pd/CNO catalyst, consequently affecting the precision and reproducibility of the proposed catalyst. These results demonstrate that both Pd/CNO and Pd/Vulcan XC-72R nanoflake catalysts have good linear response for the typical range, where glucose is found in the human body (4–8 mM) [48], thus providing a novel alternative for a possible non-enzymatic glucose sensor.

Conclusions

The RoDSE methodology was successfully employed for the deposition of Pd nanoparticles on CNOs and Vulcan XC-72R nanoflakes using the optimized conditions obtained in our previous work. The observed electrodeposition currents suggest that Pd is deposited in an equivalent manner on CNO and Vulcan XC-72R nanoflake carbon substrates. Results from Raman spectroscopy, XPS, and BET demonstrate significant differences when comparing the carbon substrates. Raman and XPS results suggest that the use of the RoDSE methodology for the deposition of Pd nanoparticles on CNOs leads to more reduction of the carbon support when compared with Vulcan XC-72R nanoflakes, thus achieving a higher degree of graphitic hybridization for CNOs. BET results showed that Pd/CNO possesses more than double the active surface area of Pd/Vulcan XC-72R nanoflakes. TEM images suggest an aggregation of smaller nanoparticles of Pd to form larger nanoparticles, hence having a high variety of sizes in the Pd/CNO samples.

The Pd/CNO catalyst exhibited improved glucose electro-oxidation when compared with Pd/Vulcan XC-72R nanoflakes with a slightly higher anodic current that results in glucose oxidation at more negative potentials. Both Pd/C catalysts demonstrated a linear correlation when comparing the anodic current response to glucose concentration. However, the Pd/CNO catalyst showed a variance of ca. 10% for the anodic current response to glucose concentration, suggesting that the conditions of the RoDSE technique for the

deposition of Pd on CNO may need to be further improve for higher precision of the Pd/CNO catalyst for glucose oxidation in alkaline media. However, considering this catalyst for a commercial glucose sensors, the U.S. Food and Drug Administration recommends between 15 and 20% of accuracy [49]. Thus, the RoDSE methodology provides a novel route for the manufacturing of high-quality Pd/C catalysts for glucose oxidation and sensing.

Funding information This work was supported by the National Science Foundation NSF-PREM: Center for Interfacial Electrochemistry of Energy Materials (CiE^2M) grant number DMR-1827622. The use of the Cornell Center for Materials Research Shared Facilities, which is supported through the NSF MRSEC grant number DMR-1719875, is greatly appreciated. LE wishes to thank the National Science Foundation, NSF-CHE 1801317, for generous support for this work and the Robert A Welch Foundation for the endowed chair, grant number AH-0033.

References

1. National Diabetes Data G (1979) Classification and diagnosis of diabetes mellitus and other categories of glucose intolerance. Diabetes 28(12):1039–1057
2. Alberti KGMM, Zimmet PZ (1998) Definition, diagnosis and classification of diabetes mellitus and its complications. Part 1: diagnosis and classification of diabetes mellitus. Provisional report of a WHO consultation. Diabet Med 15:539–553, 7
3. Toghill Richard KC (2010) Electrochemical non-enzymatic glucose sensor: a perspective and an evaluation. 5:1246–1301
4. Clark LC Jr, Lyons C (1962) Electrode systems for continuous monitoring in cardiovascular surgery. Ann N Y Acad Sci 102:29–45
5. Wang J (2008) Electrochemical glucose biosensors. Chem Rev 108(2):814–825
6. Park S, Boo H, Chung TD (2006) Electrochemical non-enzymatic glucose sensors. Anal Chim Acta 556(1):46–57
7. Updike SJ, Hicks GP (1967) The enzyme electrode. Nature 214(5092):986–988
8. Guilbault GG, Lubrano GJ (1973) An enzyme electrode for the amperometric determination of glucose. Anal Chim Acta 64(3):439–455
9. Reitz E, Jia W, Gentile M et al (2008) CuO nanospheres based nonenzymatic glucose sensor. Electroanal An Int J Devoted to Fundam Pract Asp Electroanal 20:2482–2486
10. Zhu Z, Garcia-Gancedo L, Flewitt AJ, Xie H, Moussy F, Milne WI (2012) A critical review of glucose biosensors based on carbon nanomaterials: carbon nanotubes and graphene. Sensors 12(5):5996–6022
11. Naik KK, Gangan A, Chakraborty B, Nayak SK, Rout CS (2017) Enhanced nonenzymatic glucose-sensing properties of electrodeposited $NiCo_2O_4$–Pd nanosheets: experimental and DFT investigations. ACS Appl Mater Interfaces 9(28):23894–23903
12. Hwang D-W, Lee S, Seo M, Chung TD (2018) Recent advances in electrochemical non-enzymatic glucose sensors–a review. Anal Chim Acta 1033:1–34
13. Lee W-C, Kim K-B, Gurudatt NG, Hussain KK, Choi CS, Park DS, Shim YB (2019) Comparison of enzymatic and non-enzymatic glucose sensors based on hierarchical Au-Ni alloy with conductive polymer. Biosens Bioelectron 130:48–54
14. Qiu F, Wang D, Zhu Q, Zhu L, Tong G, Lu Y, Yan D, Zhu X (2014) Real-time monitoring of anticancer drug release with highly fluorescent star-conjugated copolymer as a drug carrier. Biomacromolecules 15(4):1355–1364
15. Wang Y, Chen J, Zhou C, Zhou L, Kong Y, Long H, Zhong S (2014) A novel self-cleaning, non-enzymatic glucose sensor working under a very low applied potential based on a Pt nanoparticle-decorated TiO_2 nanotube array electrode. Electrochim Acta 115:269–276
16. Niu X, Lan M, Zhao H, Chen C (2013) Well-dispersed Pt cubes on porous Cu foam: high-performance catalysts for the electrochemical oxidation of glucose in neutral media. Chem Eur J 19(29):9534–9541
17. Lee S, Lee J, Park S, Boo H, Kim HC, Chung TD (2018) Disposable non-enzymatic blood glucose sensing strip based on nanoporous platinum particles. Appl Mater Today 10:24–29
18. Gougis M, Tabet-Aoul A, Ma D, Mohamedi M (2014) Laser synthesis and tailor-design of nanosized gold onto carbon nanotubes for non-enzymatic electrochemical glucose sensor. Sensors Actuators B Chem 193:363–369
19. Huo H, Guo C, Li G, Han X, Xu C (2014) Reticular-vein-like $Cu@Cu_2O$/reduced graphene oxide nanocomposites for a non-enzymatic glucose sensor. RSC Adv 4(39):20459–20465
20. Luo B, Li X, Yang J, Li X, Xue L, Li X, Gu J, Wang M, Jiang L (2014) Non-enzymatic electrochemical sensors for the detection of hydrogen peroxide based on Cu_2O/Cu nanocomposites. Anal Methods 6(4):1114–1120
21. Huang J, Dong Z, Li Y, Li J, Tang W, Yang H, Wang J, Bao Y, Jin J, Li R (2013) MoS_2 nanosheet functionalized with Cu nanoparticles and its application for glucose detection. Mater Res Bull 48(11):4544–4547
22. Wang X, Ge C, Chen K, Zhang YX (2018) An ultrasensitive non-enzymatic glucose sensors based on controlled petal-like CuO nanostructure. Electrochim Acta 259:225–232
23. Gao A, Zhang X, Peng X, Wu H, Bai L, Jin W, Wu G, Hang R, Chu PK (2016) In situ synthesis of $Ni(OH)_2/TiO_2$ composite film on NiTi alloy for non-enzymatic glucose sensing. Sensors Actuators B Chem 232:150–157
24. Wang Z, Hu Y, Yang W, Zhou M, Hu X (2012) Facile one-step microwave-assisted route towards Ni nanospheres/reduced graphene oxide hybrids for non-enzymatic glucose sensing. Sensors 12(4):4860–4869
25. Ye J-S, Chen C-W, Lee C-L (2015) Pd nanocube as non-enzymatic glucose sensor. Sensors Actuators B Chem 208:569–574
26. Lu L-M, Li H-B, Qu F, Zhang XB, Shen GL, Yu RQ (2011) In situ synthesis of palladium nanoparticle–graphene nanohybrids and their application in nonenzymatic glucose biosensors. Biosens Bioelectron 26(8):3500–3504
27. Li Y, Niu X, Tang J, Lan M, Zhao H (2014) A comparative study of nonenzymatic electrochemical glucose sensors based on Pt-Pd nanotube and nanowire arrays. Electrochim Acta 130:1–8
28. Chai D, Zhang X, Chan SH, Li G (2019) Facile aqueous phase synthesis of Pd3Cu–B/C catalyst for enhanced glucose electrooxidation. J Taiwan Inst Chem Eng 95:139–146
29. Moore AD, Holmes SM, Roberts EPL (2012) Evaluation of porous carbon substrates as catalyst supports for the cathode of direct methanol fuel cells. RSC Adv 2(4):1669–1674
30. Habibi B, Mohammadyari S (2015) Facile synthesis of Pd nanoparticles on nano carbon supports and their application as an electrocatalyst for oxidation of ethanol in alkaline media: the effect of support. Int J Hydrog Energy 40(34):10833–10846
31. Rodriguez-Reinoso F (1998) The role of carbon materials in heterogeneous catalysis. Carbon 36(3):159–175
32. Antolini E (2009) Carbon supports for low-temperature fuel cell catalysts. Appl Catal B Environ 88(1-2):1–24

33. Plonska-Brzezinska ME, Echegoyen L (2013) Carbon nano-onions for supercapacitor electrodes: recent developments and applications. J Mater Chem A 1(44):13703–13714
34. Palkar A, Melin F, Cardona CM et al (2007) Reactivity differences between carbon nano onions (CNOs) prepared by different methods. Chem Asian J 2(5):625–633
35. Santiago D, Rodríguez-Calero GG, Palkar A, Barraza-Jimenez D, Galvan DH, Casillas G, Mayoral A, Jose-Yacamán M, Echegoyen L, Cabrera CR (2012) Platinum electrodeposition on unsupported carbon nano-onions. Langmuir 28(49):17202–17210
36. Cunci L, Velez CA, Perez I, Suleiman A, Larios E, José-Yacamán M, Watkins JJ, Cabrera CR (2014) Platinum electrodeposition at unsupported electrochemically reduced nanographene oxide for enhanced ammonia oxidation. ACS Appl Mater Interfaces 6(3):2137–2145
37. Plonska-Brzezinska ME, Dubis AT, Lapinski A, Villalta-Cerdas A, Echegoyen L (2011) Electrochemical properties of oxidized carbon nano-onions: DRIFTS-FTIR and Raman spectroscopic analyses. ChemPhysChem 12(14):2659–2668
38. Kruk M, Jaroniec M (2001) Gas adsorption characterization of ordered organic− inorganic nanocomposite materials. Chem Mater 13(10):3169–3183
39. Kruk M, Jaroniec M, Bereznitski Y (1996) Adsorption study of porous structure development in carbon blacks. J. Colloid Interface Sci 182(1):282–288
40. Kruk M, Li Z, Jaroniec M, Betz WR (1999) Nitrogen adsorption study of surface properties of graphitized carbon blacks. Langmuir 15(4):1435–1441
41. Velez C, Corchado-Garcia J, Rojas-Pérez A et al (2017) Manufacture of Pd/carbon Vulcan XC-72R nanoflakes catalysts for ethanol oxidation reaction in alkaline media by RoDSE method. J Electrochem Soc 164(14):D1015–D1021
42. Wang F, Yang L, Tang Q, Guo Y, Hao G (2013) Synthesis of Pd/XC-72 catalysts by a facile glutamate-mediated method for solvent-free selective oxidation of DL-sec-phenethylalcohol. Catal Sci Technol 3(5):1246–1252
43. Hiura H, Ebbesen TW, Tanigaki K, Takahashi H (1993) Raman studies of carbon nanotubes. Chem Phys Lett 202(6):509–512
44. Jawhari T, Roid A, Casado J (1995) Raman spectroscopic characterization of some commercially available carbon black materials. Carbon 33(11):1561–1565
45. Blyth RIR, Buqa H, Netzer FP, Ramsey MG, Besenhard JO, Golob P, Winter M (2000) XPS studies of graphite electrode materials for lithium ion batteries. Appl Surf Sci 167(1-2):99–106
46. Khodabakhshi S, Fulvio PF, Andreoli E (2020) Carbon black reborn: structure and chemistry for renewable energy harnessing. Carbon 162:604–649
47. Chmiola J, Yushin G, Gogotsi Y, Portet C, Simon P, Taberna PL (2006) Anomalous increase in carbon capacitance at pore sizes less than 1 nanometer. Science 313(5794):1760–1763
48. Heller A (1999) Implanted electrochemical glucose sensors for the management of diabetes. Annu Rev Biomed Eng 1(1):153–175
49. U.S. Department of Health and Human Services Food and Drug Administration Center for Devices and Radiological Health (2016) Self-monitoring blood glucose test systems for over-the-counter use